

# Room-Temperature Synthesis of 2D Janus Crystals and their Heterostructures

Dipesh B. Trivedi, Guven Turgut, Ying Qin, Mohammed Y. Sayyad, Debarati Hajra, Madeleine Howell, Lei Liu, Sijie Yang, Naim Hossain Patoary, Han Li, Marko M. Petrić, Moritz Meyer, Malte Kremser, Matteo Barbone, Giancarlo Soavi, Andreas V. Stier, Kai Müller, Shize Yang, Ivan Sanchez Esqueda, Houlong Zhuang, Jonathan J. Finley, and Sefaattin Tongay\*

Janus crystals represent an exciting class of 2D materials with different atomic species on their upper and lower facets. Theories have predicted that this symmetry breaking induces an electric field and leads to a wealth of novel properties, such as large Rashba spin-orbit coupling and formation of strongly correlated electronic states. Monolayer MoSSe Janus crystals have been synthesized by two methods, via controlled sulfurization of monolayer MoSe<sub>2</sub> and via plasma stripping followed thermal annealing of MoS<sub>2</sub>. However, the high processing temperatures prevent growth of other Janus materials and their heterostructures. Here, a room-temperature technique for the synthesis of a variety of Janus monolayers with high structural and optical quality is reported. This process involves low-energy reactive radical precursors, which enables selective removal and replacement of the uppermost chalcogen layer, thus transforming classical transition metal dichalcogenides into a Janus structure. The resulting materials show clear mixed character for their excitonic transitions, and more importantly, the presented room-temperature method enables the demonstration of first vertical and lateral heterojunctions of 2D Janus TMDs. The results present significant and pioneering advances in the synthesis of new classes of 2D materials, and pave the way for the creation of heterostructures from 2D Janus layers.

Named after the two-faced Roman god, Janus crystals are a new class of 2D materials that contain different atoms/composition on each side of their unit cell and thus break the mirror symmetry<sup>[1]</sup> (Figure 1). Due to the large electronegativity difference across their unit-cells, these materials are expected to host substantial vertical polarization fields.<sup>[1–3]</sup> Considering the discoveries made by the effects of electric field and broken crystal symmetry in the past, there is significant scientific interest in these materials. For example, it has recently been theoretically predicted that colossal polarization in 2D layers leads to high Curie temperature ( $T_c$ ) ferromagnetic order,<sup>[4,5]</sup> skyrmion formation,<sup>[6]</sup> giant Rashba splitting,<sup>[1]</sup> and unique excitonic behavior.<sup>[7,8]</sup> Especially when these 2D Janus layers are assembled in vertical and lateral heterostructures configurations, it allows one to access exotic material properties such as magnetic ordering, rich exciton complexes, electric-field-driven catalysis, and

D. B. Trivedi, Dr. G. Turgut, Y. Qin, M. Y. Sayyad, D. Hajra, M. Howell, L. Liu, Dr. S. Yang, N. H. Patoary, H. Li, Dr. S. Yang, Prof. I. S. Esqueda, Prof. H. Zhuang, Prof. S. Tongay

School of Electrical, Computer, and Energy Engineering  
Arizona State University

Tempe, AZ 85287, USA  
E-mail: sefaattin.tongay@asu.edu

M. M. Petrić, M. Meyer, Dr. M. Barbone, Prof. K. Müller  
Walter Schottky Institut  
Department of Electrical and Computer Engineering and MCQST  
Technische Universität München  
Am Coulombwall 4, Garching 85748, Germany

The ORCID identification number(s) for the author(s) of this article  
can be found under <https://doi.org/10.1002/adma.202006320>.

DOI: 10.1002/adma.202006320

M. Kremser, Dr. A. V. Stier, Prof. J. J. Finley  
Walter Schottky Institut

Physik Department and MCQST  
Technische Universität München  
Am Coulombwall 4, Garching 85748, Germany

Prof. G. Soavi  
Institut für Festkörperphysik  
Friedrich-Schiller-Universität Jena  
Max-Wien-Platz 1, Jena 07743, Germany

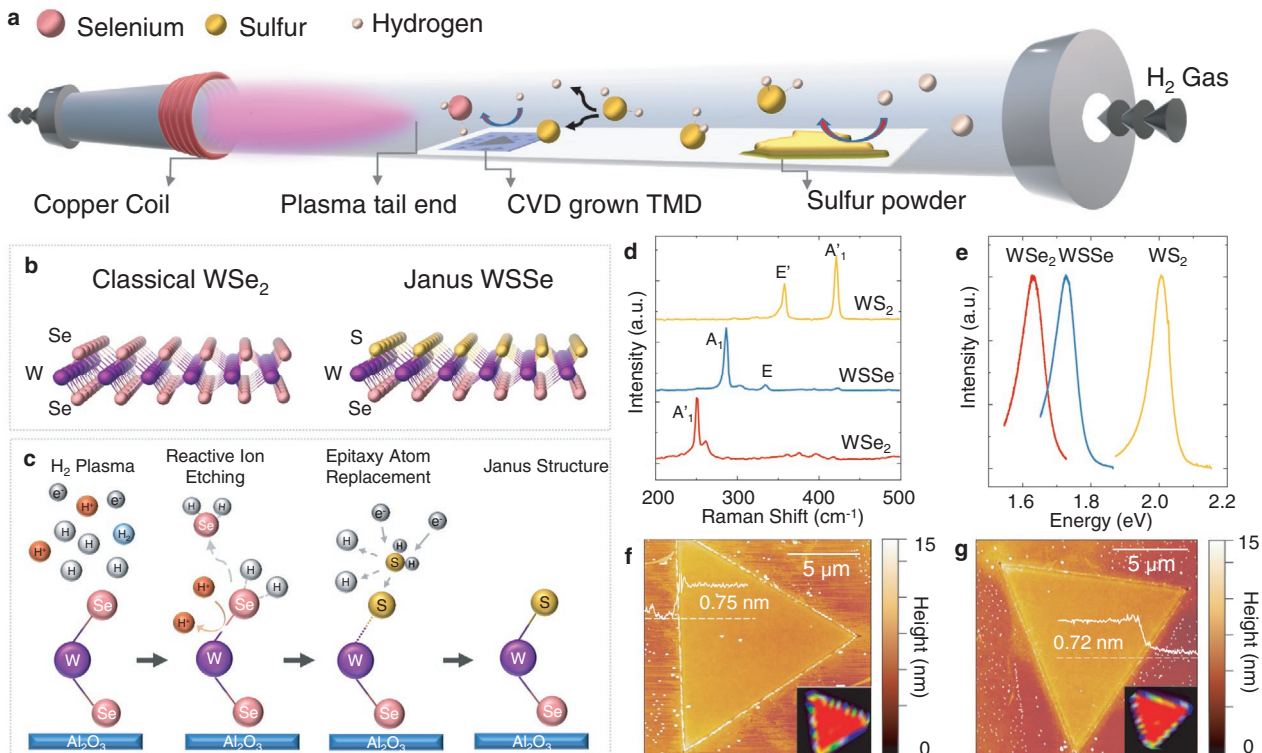


**Figure 1.** a) Schematic demonstration of the SEAR process through inductively coupled plasma. b) The crystal structure of WSe<sub>2</sub> monolayer and WSSe monolayer. c) Working scheme of room-temperature SEAR process. d) Raman spectra comparison of WSe<sub>2</sub>, WS<sub>2</sub>, and WSSe with FWHM of most prominent peaks being 5.5, 5.1, and 4.4 cm<sup>-1</sup>, respectively. e) Photoluminescence spectra of WSe<sub>2</sub>, WSSe, and WS<sub>2</sub> with FWHM being 115, 92, and 80 meV, respectively. f,g) AFM profile of WSe<sub>2</sub> before (f) and after (g) the SEAR process. Inset: Raman mapping of peaks at 250 cm<sup>-1</sup> (WSe<sub>2</sub> A<sub>1</sub>' mode) and 284 cm<sup>-1</sup> (WSSe A<sub>1</sub> mode), respectively.

spintronic responses simply by engineering the polarization architecture vertically across the layers or laterally across the grain boundaries.<sup>[9–11]</sup>

Despite these exciting theoretical predictions, there are limited experimental studies to date, mainly due to the challenges in 2D Janus synthesis, sample preparation, and limited material quality. The prime difficulty presented in the synthesis of these Janus materials is that they are thermodynamically unstable in their bulk form, with the exception of the BiTeI family.<sup>[12]</sup> While the creation of thermodynamically stable 2D alloys is easier,<sup>[13]</sup> Janus layers, unlike their alloy counterparts, must be produced at unit cell level with atomic precision. Because of these problems—to the best of our knowledge—there are only three approaches<sup>[2,7,14]</sup> recently reported in the literature. The first method replaced the top selenium layer in MoSe<sub>2</sub> in the presence of sulfur vapor (S<sub>2</sub>) at a high temperature (800 °C) to produce Janus MoSSe.<sup>[2]</sup> In the other method by Lu et al.,<sup>[7]</sup> the sulfur layer was removed using a hydrogen (H<sub>2</sub>) plasma, and selenium atoms were decorated on the surface at an elevated temperature (450 °C). The third method relied on low energy implantation of Se atoms in WS<sub>2</sub> to form Janus WSSe at 300 °C.<sup>[14]</sup> These methods require processing well above room temperature. While this is welcome in the traditional semiconductor industry, it is highly undesirable for the production of 2D Janus layers. First, any finite temperature processing will increase the risk of converting thermodynamically unfavorable 2D Janus layers into more favorable 2D alloys.

Moreover, any two-step process involving finite temperature is known to introduce chalcogen vacancies in classical transition metal dichalcogenides (TMDs)<sup>[15]</sup> as well as 2D Janus layers.

Here, we report a room-temperature synthesis method of 2D Janus TMDs and the vertical and lateral heterostructures of these 2D Janus TMDs by a selective epitaxy atomic replacement (SEAR) process. The growth starts with chemical vapor deposited (CVD) MSe<sub>2</sub> (M = W, Mo), and the operation relies on the formation of selenium vacancies (V<sub>Se</sub>) by hydrogen radicals created through inductively coupled plasma (ICP), and substitution by sulfur atoms in the presence of low-energy reactive sulfur radicals. The present technique differs in that the replacement process is driven kinetically not thermally: the chalcogen vacancies are created and low energy chalcogen radicals are utilized to decorate different chalcogen atoms on the surface to form 2D Janus layers. Our studies demonstrate selective removal of the top chalcogen layer and subsequent replacement with sulfur or other chalcogens by tight control over the kinetic energy of radical species with respect to the metal-chalcogen bond energy. Another significant benefit offered by this technique is that the entire process takes place at room temperature. This key aspect allows the formation of 2D Janus heterostructures without running into thermal degradation/decomposition issues.

Our Janus growth process starts with CVD of 2D MoSe<sub>2</sub> and WSe<sub>2</sub> TMDs using established techniques in the literature.<sup>[16–19]</sup> The as-grown MoSe<sub>2</sub> and WSe<sub>2</sub> monolayers were loaded into a 1-in. diameter quartz tube at ≈300 mTorr pressure in the

presence of high purity 20 sccm H<sub>2</sub> gas. The samples were kept ≈4 cm upstream from the plasma glow as schematically shown in Figure 1a. ICP was generated by supplying 15W RF power at 13.56 MHz frequency to a copper coil which ionizes and dissociates H<sub>2</sub> molecules into H<sup>+</sup> ions and H free radicals. The concentration of ionized species and the extent of the plasma tail is controlled through the RF power. In the process of Janus WSSe conversion from WSe<sub>2</sub>, H radicals are first adsorbed on WSe<sub>2</sub> and form weak bonds with the top Se atoms, creating intermediate species. Highly energetic H<sup>+</sup> ions bombard and knock-off these intermediates, which result in Se vacancies as well as H<sub>2</sub>Se/HSe<sup>+</sup> byproducts, as established in the literature<sup>[20,21]</sup> (Figure 1c). The remaining metastructure consists of densely packed metal atoms and lower chalcogen layer which respond to atomic level changes in the surface by potential reconstruction of their bonds. As such, we argue that the kinetic energy of H radicals is not high enough to penetrate the metal network layer and prohibits its reaction with the lower chalcogen atoms due to higher bond energy as well as higher chemical potential cost. In our studies, we find that the distance from the plasma tail and exposure time ultimately dictates the Se vacancy generation rate; when increasing the distance beyond the ideal position, vacancy creation becomes inefficient and prevents Janus structure formation. Similarly, moving samples closer to the plasma tail exposes monolayers to energetic ions and results in heavily defected samples (Figure S1b,c, Supporting Information).

The crucial part of the Janus synthesis is the introduction of sulfur (Figure 1a) upstream from the TMDs sample in the SEAR process, which helps in the effective incorporation of sulfur atoms into plasma stripped WSe<sub>2</sub> monolayers without any thermal assistance. Since the dissociation energy is much lower than the required energy for ionization (Table S1, Supporting Information, and Figure 1c), the extent of H-free radicals is far beyond the visible plasma glow, which results in the formation of H<sub>2</sub>S vapor near the sulfur through a similar reaction process described above. We hypothesize that the H<sub>2</sub>S molecules are then transported toward the TMD sample by the gas flow and dissociate into individual radical species of S and H (by higher RF power). S radicals then incorporate into the chemically active V<sub>Se</sub> sites to form a stable WSSe Janus structure. The Se etching and S replacement processes happen simultaneously and continue until all the upper Se are replaced by S. Well-optimized processing times and sufficient supply of sulfur (in the form of H<sub>2</sub>S or S radicals) are required to prevent over-etching, to stabilize the Janus structure, and to create highly crystalline Janus layers as demonstrated in Figure S2, Supporting Information. Based on over 200 growth studies, we found it easier to incorporate S into V<sub>Se</sub> and retain S on that site without further etching as the metal-sulfur bonds are stronger compared to metal-selenium ones. Likewise, the processing time required for W-based TMDs is longer compared to Mo-based TMDs due to higher cohesive energy.<sup>[22]</sup> This suggests that the relation between radical species, plasma properties, and metal-chalcogen bonds plays a significant role in the efficacy of the Janus monolayer fabrication and merit more systematic studies using industrial grade plasma systems. The quality of Janus WSSe can be assessed from the narrow FWHM of the Raman spectra (FWHM ≈5.1 cm<sup>-1</sup>) and strong PL emission as

shown in Figure 1d,e and as will be discussed in detail below. It is noteworthy that the surface of WSe<sub>2</sub> remains pristine even after Janus WSSe fabrication, as evident from AFM scans in Figure 1f,g. These datasets mark the experimental realization of Janus WSSe at room temperature and demonstrate the feasibility of the SEAR approach.

To confirm the structure produced with the SEAR process is indeed Janus, Scanning Transmission Electron Microscopy (STEM) medium angle annular dark field (MAADF) images of the monolayer were taken at a tilted angle to reveal the underlying chalcogen atoms.<sup>[23,24]</sup> The monolayer WSSe sample was tilted by 21° along the horizontal direction with respect to out-of-plane c direction and the MAADF images are shown in Figure 2a. Image simulations at the same tilt angle were carried out with structural models of WSSe Janus (Figure 2b) and WSe<sub>2</sub> monolayers (Figure 2c). It is shown that both layers of chalcogen atoms are visible with this tilt angle and a sharp contrast is observed between S and Se due to the Z-contrast STEM imaging. The absence of double Se sites from our experimental image in Figure 2a confirms the selective replacement of top selenium layer with sulfur atoms. Furthermore, the tilted images also reveal highly ordered arrangement of chalcogen atoms, which confirms that the SEAR technique forms Janus structure and not an amalgamation of sulfur atoms to form alloy.

To verify the asymmetric chalcogen atoms distribution in a quantitative way, we show the line profile of intensity across non-tilted MAADF images of the sample (Figure 2d), compared with the non-tilted image simulation of Janus WSSe (Figure 2e) and WSe<sub>2</sub> (Figure S6d, Supporting Information). The line profile in Figure 2f shows that experimental data agrees with the simulation of Janus WSSe and contrasts with WSe<sub>2</sub>. These results, in addition with optical spectra, provide strong direct evidence of the formation of Janus monolayer.

**Figure 3** shows the Raman and photoluminescence (PL) spectra of homogenous WSSe and MoSSe grown via the room-temperature SEAR technique. As shown in Figure 3a, Janus MoSSe and WSSe exhibit different Raman spectra when compared with their parent TMD materials (i.e., MoS<sub>2</sub>, MoSe<sub>2</sub>, WS<sub>2</sub>, and WSe<sub>2</sub>). The observed Raman spectra also differ significantly from 2D alloy WSSe<sup>[25]</sup> and MoSSe<sup>[26,27]</sup> (see Figure S3, Supporting Information). Moreover, our calculated vibrational dispersion, together with the published predictions for WSSe and MoSSe<sup>[7,8,14,28]</sup> match reasonably well with our experimental datasets with a deviation of around 1.1–2.8%, as shown in Figures S4 and S5, Supporting Information, and **Table 1**. These observations again validate that the as-synthesized layers have Janus structure instead of random alloying.

Overall, 2D Raman maps at the characteristic Janus vibrational mode frequency (284 cm<sup>-1</sup> for WSSe and 290 cm<sup>-1</sup> for MoSSe) show a remarkable uniformity across the synthesized 2D Janus layers (Figure 3b,c). More importantly, the FWHM of the synthesized 2D Janus TMDs reaches as low as ≈5.1 cm<sup>-1</sup>. These values are much smaller compared to Janus MoSSe produced by the aforementioned techniques<sup>[2,7]</sup> and comparable to high-quality conventional TMDs crystals. Fast Fourier transform of HAADF STEM images collected from Janus WSSe monolayers also shows that the crystal structure remains in the hexagonal symmetry and retains its

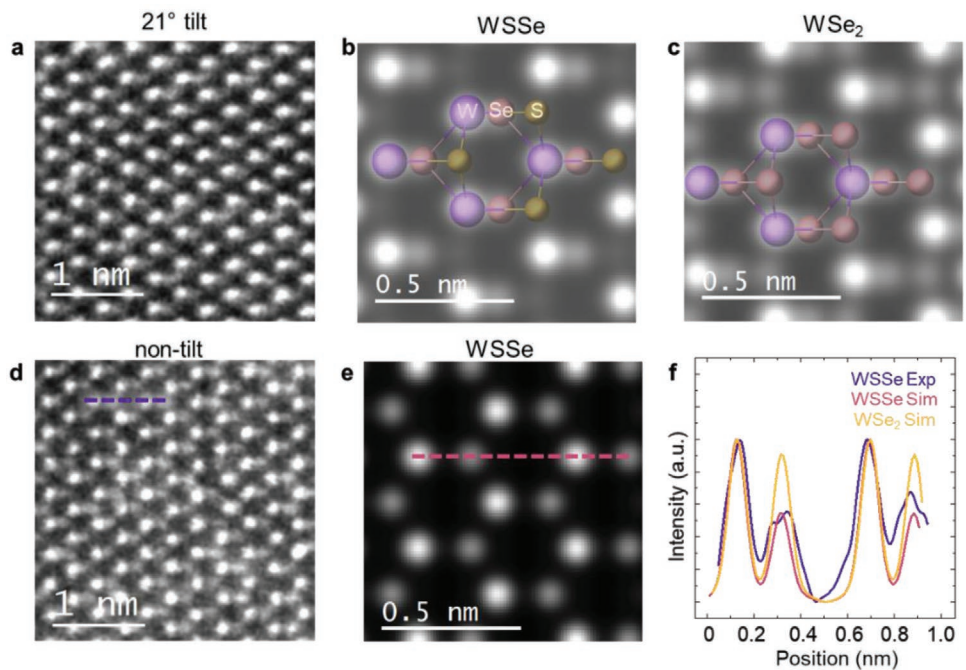


**Figure 2.** a) STEM-MAADF image of Janus WSSe monolayer tilted at 21°. b) WSSe structure overlaid on image simulated at this tilt angle and c) WSe<sub>2</sub> structures and image simulated at 21°. d,e) STEM-MAADF image of non-tilted Janus WSSe monolayer and corresponding simulation. f) Line profile of intensity from (d), (e), and WSe<sub>2</sub> image simulation (Figure S6d, Supporting Information).

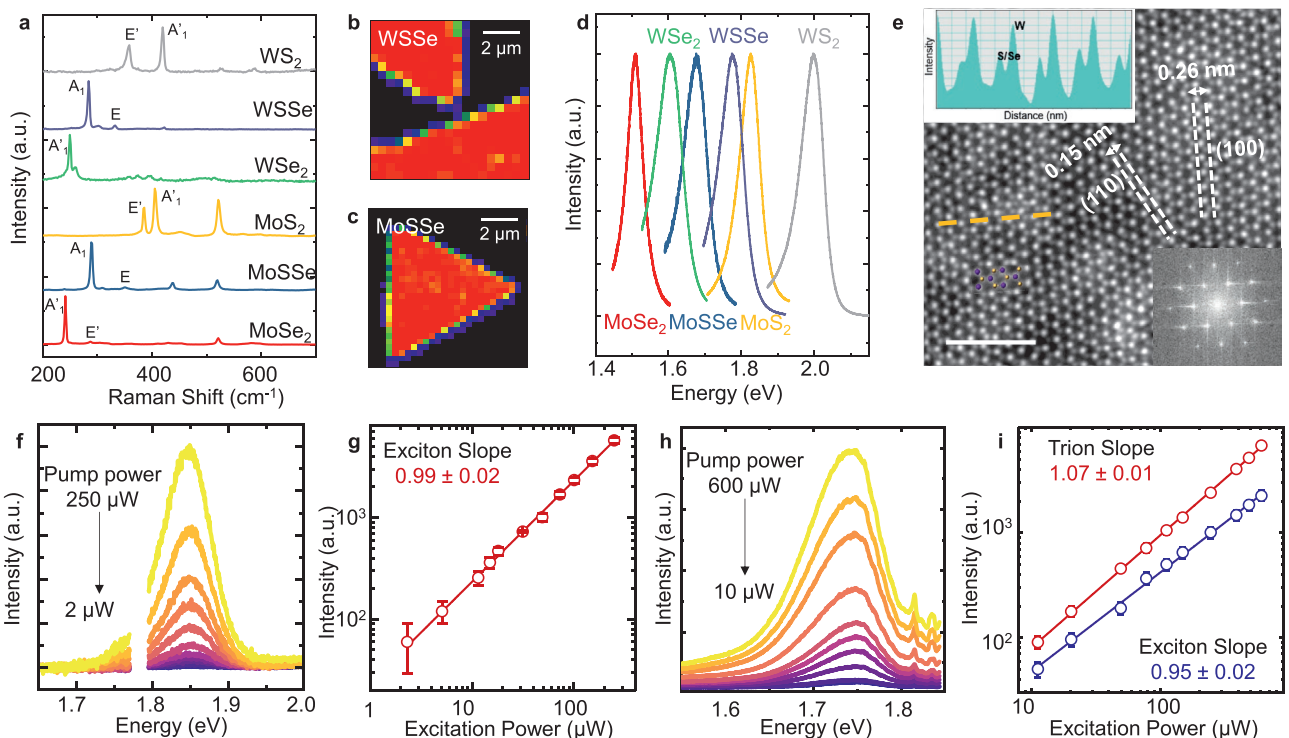


**Figure 3.** a) Raman spectra from Janus MoSSe, WSSe, and their parent TMD structures. b) Raman mapping of WSSe and c) MoSSe at 284 and 290 cm<sup>-1</sup>, respectively. d) PL of MoSSe, WSSe, and their parent TMD structures. e) HAADF STEM image of WSSe showing hexagonal lattice structure and spacing of (100) and (110) planes, top left inset shows line profile along the yellow dashed line; bottom right inset shows FFT image. f,h) Power-dependent PL of WSSe and MoSSe at 10 K. g,i) Fitted power dependence of peak intensity versus excitation power of WSSe and MoSSe, respectively.

**Table 1.** Comparison between experimental and theoretical values of Raman active vibrational modes for Janus MoSSe and WSSe.

Material	$A_1$ (Experiment)	$A_1$ (Theory)	E (Experiment)	E (Theory)
Janus WSSe	284 cm <sup>-1</sup>	276 cm <sup>-1</sup>	331 cm <sup>-1</sup>	323 cm <sup>-1</sup>
Janus MoSSe	290 cm <sup>-1</sup>	287 cm <sup>-1</sup>	351 cm <sup>-1</sup>	347 cm <sup>-1</sup>

crystallinity after SEAR processing, as shown in Figure 3e for Janus WSSe and Figure S7, Supporting Information, for Janus MoSSe.

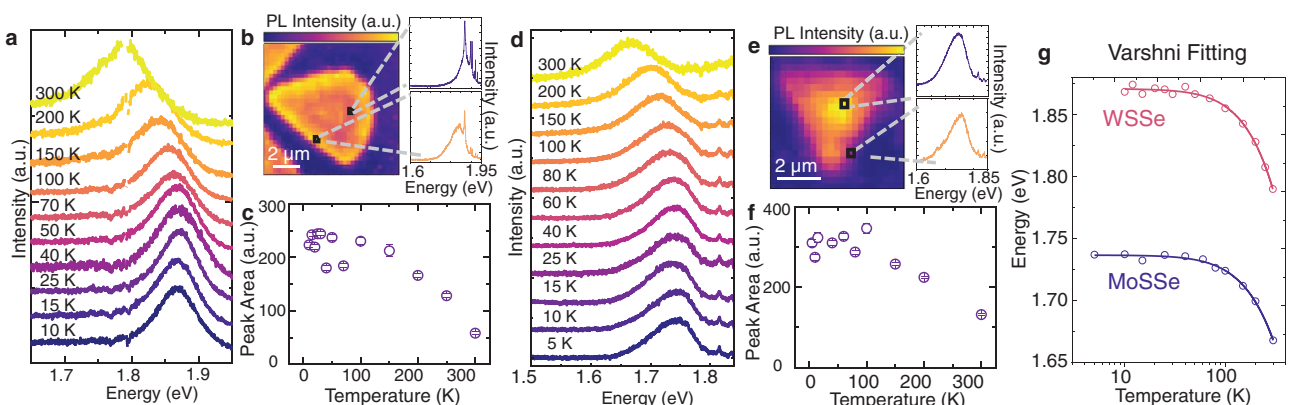
The measured PL spectra in Figure 3d substantiate the high crystal quality. The PL intensity is similar to that of CVD grown classical TMDs (See Figure S8, Supporting Information) and the PL FWHM is at least 30–40% sharper compared to the PL from Janus crystals produced by high-temperature methods. PL mapping (see Figure S9, Supporting Information) shows overall uniform intensity across the samples. The emission energy of the 2D Janus WSSe and MoSSe at 10 K is 1.85 and 1.75 eV, respectively, and at room temperature, they measure 1.78 and 1.68 eV respectively. The excitonic nature of these PL peaks is apparent from the power dependence shown in Figure 3f–i. The PL intensity of WSSe yields an almost linear slope ( $\alpha \approx 0.99$ ), suggesting monomolecular (excitonic) recombination processes. As shown for 2D Janus MoSSe in Figure 3h and Figure S10, Supporting Information, we note that some of the PL spectra collected are broader and asymmetric, which we interpret as the convolution of at least two peaks. Power-dependent emission shows that the intensity of the low energy peak has a higher slope with excitation power (exponent  $\approx 1.07 \pm 0.01$ ) than the high-energy peak (slope  $\approx 0.95 \pm 0.02$ ), thus suggesting the presence of coexisting many-body states, possibly trions, and neutral excitons.<sup>[29,30]</sup>

Temperature-dependent PL measurements on 2D Janus WSSe and MoSSe layers (Figure 4) show two main effects. First, the position of the PL peak is fitted with a Lorentzian function and the PL peak positions show a hypsochromic shift at lower temperatures (shown in Figure 4a–d), and the PL line shape becomes narrower (95 meV at 300 K  $\rightarrow$  60 meV at 10 K for WSSe). Here, the variation of the PL peak position with tem-

perature (Figure 4g) can be well-explained within the Varshni law<sup>[31]</sup>  $E_g(T) = E_g(0) - \frac{\alpha T^2}{T + \beta}$  which has been successfully used for traditional semiconductors as well as 2D MoSe<sub>2</sub><sup>[32,33]</sup> and WSe<sub>2</sub>.<sup>[34]</sup> Typical Varshni fitting process offers excellent fit with  $E_g(0) = 1.87$  eV,  $\alpha = 5.09 \times 10^{-4}$  eV/K,  $\beta = 260.02$  K for WSSe and  $E_g(0) = 1.74$  eV,  $\alpha = 3.95 \times 10^{-4}$  eV/K,  $\beta = 216.71$  K for MoSSe. Second, the integrated PL peak intensity increases with decreasing temperature as shown in Figure 4c–f. This behavior is suggesting a bright exciton ground state which is completely opposite to what is found for W-based classical TMDs and warrants further studies.<sup>[35–37]</sup>

Figure 4b–e show the overall PL emission intensity across an entire 2D Janus crystal. Some of the layers exhibit edge PL enhancement effect,<sup>[38]</sup> as shown in Figure 4b for WSSe and S8 for MoSSe. PL mapping at low temperatures reveals that the PL emission intensity and wavelength have some degree of variation across the sample. Our PL spectra collected from the edges and the other segments of the 2D Janus layers show that PL peak shifts by  $\Delta E \approx 40$  meV. This  $\Delta E$  value is comparable with the ionization energy of charged excitons observed in classical TMDs ( $\approx 20$ –40 meV), suggesting an interplay between neutral and charged exciton complexes.<sup>[29]</sup> The outer regions of the Janus monolayers may have a higher defect density and a different charge-doping distribution compared to the central region, which increases photoluminescence at these positions as well as shifts the emission energy. This defect and charge inhomogeneity may arise from a non-uniform substitution of the selenide atoms during the growth process, which could further explain the observed PL intensity and emission energy pattern. Here, we also note that the synthesized 2D Janus TMDs exhibit field-effect-transistor (FET) performance much similar to those in classical TMDs demonstrating its electrical grade (Figure S14, Supporting Information).

Owing to the mild processing conditions of our ambient temperature synthesis, we next demonstrate the first-of-a-kind realization of lateral and vertical heterostructures of 2D Janus layers in Figure 5. So far, theoretical studies have identified that vertical and lateral heterostructures of 2D Janus layers offer unique quantum effects and functionalities.<sup>[8–11,39,40]</sup> Despite strong theoretical interest in these sophisticated structures,

**Figure 4.** a) Temperature-dependent PL spectra (300–10 K). b) PL mapping (10 K) and c) PL peak intensity (integrated area) versus temperature for Janus WSSe. d–f) Similar data recorded for Janus MoSSe. g) Varshni fitting of PL peak position of Janus MoSSe and WSSe layers with respect to temperature.

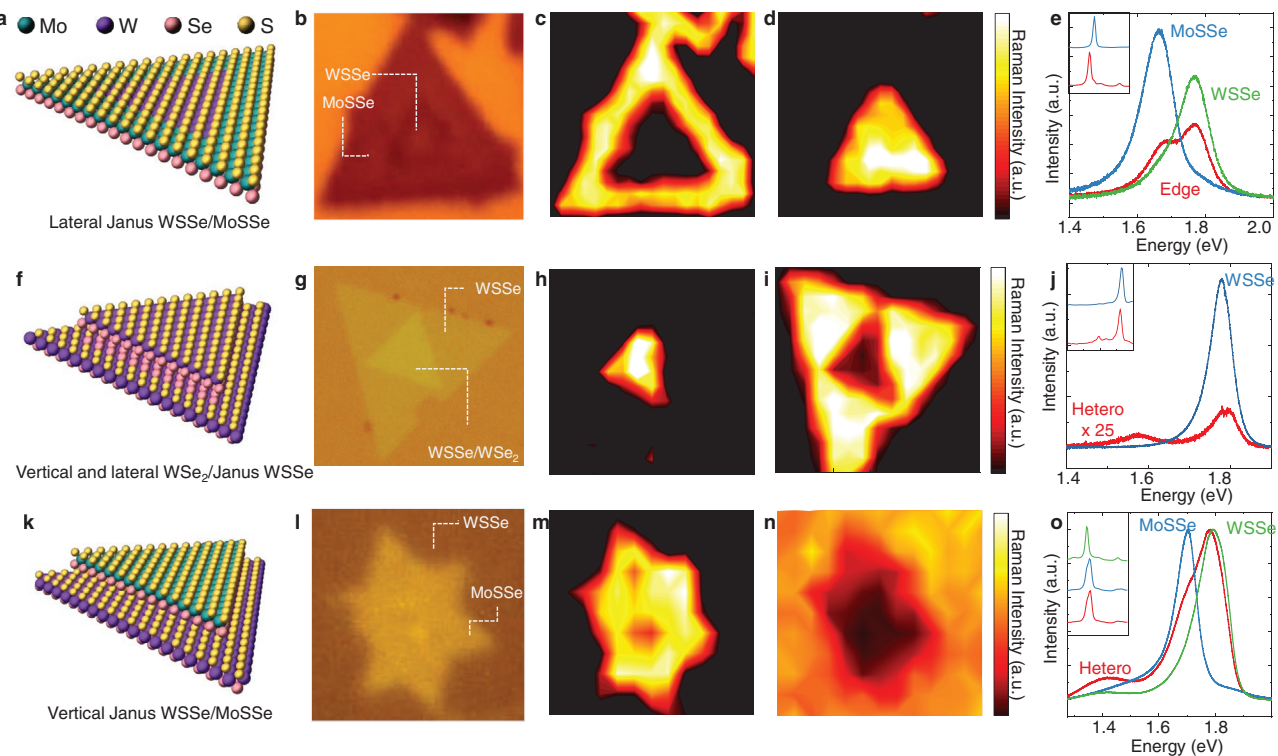


**Figure 5.** a) The atomic representation and b) optical image of Janus MoSSe/WSSe lateral heterostructures. c,d) Raman mapping at  $290$  and  $284\text{ cm}^{-1}$  for characteristic Janus MoSSe and WSSe peaks. e) PL comparison on MoSSe, WSSe, and at the interface. Inset: Raman measured (range  $250$ – $350\text{ cm}^{-1}$ ) from edge MoSSe and center WSSe. f) The atomic representation, and g) the optical image of Janus WSe<sub>2</sub>/Janus WSSe, vertical heterostructure. h,i) Raman mapping of WSe<sub>2</sub> at  $250\text{ cm}^{-1}$  and WSSe at  $284\text{ cm}^{-1}$ . j) PL comparison between edge WSSe area and center WSe<sub>2</sub>/WSe<sub>2</sub> area. Inset: Raman (range  $200$ – $300\text{ cm}^{-1}$ , normalized) comparison from edge Janus WSSe and center vertical WSe<sub>2</sub>/WSe<sub>2</sub> heterostructure. k) The atomic representation and l) the optical image of vertical Janus MoSSe/WSSe heterostructure. m,n) Raman mapping of MoSSe at  $290\text{ cm}^{-1}$  and WSSe peak  $284\text{ cm}^{-1}$ . o) PL spectra collected from Janus MoSSe, WSSe, and their vertical heterostructures. The full range of Raman spectra collected from these heterostructures is shown in Figure S12, Supporting Information.

their synthesis has not been realized using other high-temperature processing techniques. The difficulty presented by the previous methods is that at high temperatures, it is easier to deteriorate one of the constituent materials, or it is more likely to form an alloy instead of 2D Janus layers. The SEAR process aims to circumvent this fundamental challenge. Figure 5a shows the schematic description of a WSSe/MoSSe lateral heterostructure. Here, we note that these 2D Janus TMDs heterostructures are completely different from heterostructures of 2D classical TMDs such as MoS<sub>2</sub>/WS<sub>2</sub>.

Our process starts with established CVD growth of 2D WSe<sub>2</sub>/MoSe<sub>2</sub> lateral junctions using a two-step growth synthesis with MoO<sub>3</sub>, WoO<sub>3</sub>, and Se precursors.<sup>[41]</sup> Since deposition temperature for the WSe<sub>2</sub> monolayers is higher, they are synthesized first, followed by the growth of MoSe<sub>2</sub> on their edges at a lower temperature. We carried out our established ambient temperature SEAR process on as-synthesized WSe<sub>2</sub>/MoSe<sub>2</sub> to produce Janus lateral heterostructures (Figure 5a). Raman mapping (Figure 5c,d) at characteristic MoSSe A<sub>1</sub> peak ( $290\text{ cm}^{-1}$ ) and WSSe A<sub>1</sub> peak ( $284\text{ cm}^{-1}$ ) confirm the formation of a Janus WSSe/MoSSe lateral heterostructures with WSSe monolayer as the core and MoSSe monolayer being the outer shell. Similarly, PL spectra acquired from the outer domain (blue spectra) and inner domain (green spectra in Figure 5e) show characteristic

PL peaks of 2D Janus MoSSe ( $\approx 1.68\text{ eV}$ ) and WSSe ( $\approx 1.78\text{ eV}$ ), and the PL position mapping also reveals the core-shell structure of this unique lateral heterostructure as shown in Figure S11, Supporting Information. The PL collected at the MoSSe/WSSe interface shows that emission from individual domains is superimposed onto each other (red spectra) since the probing spot ( $1\text{ }\mu\text{m}$ ) is much larger than the exciton wavefunction. The presented results, enabled by this simple, scalable, and surface limited growth process, introduce the 2D Janus lateral heterostructures shown in Figure 5a–e.

While 2D Janus lateral heterostructures can easily be created, the synthesis of vertical heterostructures has restrictions due to the surface-limited nature of the SEAR process. For instance, when CVD-grown bilayer WSe<sub>2</sub>, consisting of a larger monolayer base and a smaller WSe<sub>2</sub> triangle on top, undergoes our SEAR process (Figure 5f–j), we find that the exposed selenium atoms are successfully replaced with sulfur. However, selenium atoms covered by the smaller WSe<sub>2</sub> triangle remain unaffected. As a result, the final structure has both vertical WSe<sub>2</sub>/Janus WSSe and lateral WSSe/WSe<sub>2</sub> heterostructures (Figure 5f). Raman mapping at  $250\text{ cm}^{-1}$  in Figure 5h shows that the underlying WSe<sub>2</sub> layer remains in the central triangular region. This suggests that the SEAR process is surface limited, and the reactive chalcogen or hydrogen radicals cannot intercalate

between the layers. Since sulfur atoms successfully replaced all the exposed selenium atoms, the  $284\text{ cm}^{-1}$  peak for Janus WSSe can be found across the entire sample (Figure 5i). Here, the central segment shows a slightly lower  $284\text{ cm}^{-1}$  WSSe peak intensity. The observed Raman reduction in both WSSe and WSe<sub>2</sub> Raman signal on the vertical heterostructure is most likely related to the presence of interlayer coupling between WSe<sub>2</sub> and Janus WSSe layers, much like those observed in the classical bilayer and trilayer TMDs<sup>[42]</sup> (Figure S13, Supporting Information).

To form truly 2D Janus vertical heterostructures and to further demonstrate the capability of the SEAR process, we have transferred monolayer MoSe<sub>2</sub> on Janus WSSe monolayers (MoSe<sub>2</sub>/WSSe) using polymer assisted techniques<sup>[43,44]</sup> before the SEAR process. During the conversion process, the exposed selenium atoms on the MoSe<sub>2</sub> monolayer got replaced by the sulfur atoms, but the underlying Janus WSSe layer, as well as exposed (monolayer) regions, remained intact to form 2D Janus MoSSe/WSSe vertical heterostructure. Raman intensity mapping using the MoSSe A<sub>1</sub> mode at  $290\text{ cm}^{-1}$  and the WSSe A<sub>1</sub> mode at  $284\text{ cm}^{-1}$  demonstrate the formation of MoSSe/WSSe bilayer stacks as shown in Figure 5k-o. The MoSSe signal is observed only from the central segment of the sample, while the other regions mainly yield WSSe related Raman peak. This suggests that it is possible to form MoSSe/WSSe vertical junctions starting with classical/Janus vertical heterolayers, followed by the SEAR process. The PL spectra (Figure 5o blue and green) acquired from the monolayer regions show sharp peaks at 1.68 and 1.78 eV, respectively, corresponding to the direct excitonic transition energy in monolayer Janus MoSSe and WSSe. PL spectra collected from the bilayer MoSSe/WSSe region show that these two peaks coexist with each other.

In summary, we demonstrate the growth of high-quality 2D Janus layers and their vertical and lateral heterostructures using all room-temperature SEAR technique. This technique allows us to synthesize 2D Janus layers as well as their complex heterostructures, namely, lateral WSe/MoSSe, vertical MoSSe/WSSe, and Janus/classical MoSSe/MoS<sub>2</sub> which were not possible prior to this work. Overall, our technique offers significant advances to the synthesis and fabrication of 2D Janus materials and enables their combination in heterostructures without sacrificing structural or optical quality, thus providing a much-needed platform for the study of unique physical phenomena and further unlocking the transfer of exciting properties into cutting-edge applications.

## Experimental Section

**Chemical Vapor Deposited Growth of Transition Metal Dichalcogenides:** The synthesis of monolayer MoSe<sub>2</sub> was achieved via ambient pressure chemical vapor deposition (AP-CVD) method previously reported in the literature.<sup>[18]</sup> 2 mg of MoO<sub>3</sub> precursor (Sigma-Aldrich, ≥99.5% purity) mixed with NaCl in a 50:1 ratio was placed in a ceramic boat at the center of a Lindberg/Blue M Tube furnace. 285 nm SiO<sub>2</sub>/Si substrates, the polished side facing downward, were placed on the ceramic boat. Selenium precursor was placed upstream in a ceramic crucible in excess, where the temperature was maintained at 300 °C. High purity Ar (≥99.99%) and H<sub>2</sub> were passed at 46 and 4 sccm flow rates, respectively, during the entire growth process. The furnace was ramped up with a rate of  $30\text{ °C min}^{-1}$  to 760 °C and held at 760 °C for 13 min before natural cooling to room temperature.

The synthesis of monolayer/bilayer MoS<sub>2</sub> was achieved via AP-CVD method.<sup>[18]</sup> 1 mg of MoO<sub>3</sub> precursor mixed with NaCl in 50:1 ratio was placed in a ceramic boat at the center of the single-zone tube furnace. 285 nm SiO<sub>2</sub>/Si substrates were placed polished side down on the ceramic boat. Sulfur was placed upstream in a ceramic crucible in excess, where the temperature was maintained at 200 °C. High purity Ar was passed at 20 sccm during the entire growth process. The furnace was ramped up with a rate of  $30\text{ °C min}^{-1}$  to 700 °C and held for 13 min before naturally cooling to room temperature.

The synthesis of monolayer WSe<sub>2</sub> was achieved via AP-CVD method.<sup>[19]</sup> 60 mg of WO<sub>3</sub> precursor was placed in a ceramic boat at the center of the single-zone tube furnace. Double side polished sapphire substrates were placed on the ceramic boat. Selenium powder was placed upstream in a ceramic crucible in excess, where the temperature was maintained at 250 °C. High-purity Ar (≥99.99%) and H<sub>2</sub> gas were passed at 36 and 4 sccm flow rates, respectively, during the entire growth process. The furnace was ramped up with a rate of  $30\text{ °C min}^{-1}$  to 850 °C and held at 850 °C for 20 min before natural cooling to room temperature.

The synthesis of monolayer WS<sub>2</sub> was achieved via AP-CVD method.<sup>[45]</sup> 50 mg of WO<sub>3</sub> precursor was placed in a ceramic boat at the center of the single-zone tube furnace. Double side polished sapphire substrates were placed on the ceramic boat. The sulfur powder was placed upstream in a ceramic crucible in excess, where the temperature was maintained at 250 °C. High purity Ar (≥99.99%) and H<sub>2</sub> gas were passed at 50 and 1.5 sccm flow rates, respectively, during the entire growth process. The furnace was ramped up with a rate of  $15\text{ °C min}^{-1}$  to 870 °C and gradually cooled to 760 °C in 40 min before natural cooling to room temperature.

**Selective Epitaxy Atomic Replacement:** Creation of Janus TMDs with the SEAR method was carried out in a home-built ICP setup, the details of which are depicted in Figure S1a, Supporting Information. A 5-foot long quartz tube with 1-in. diameter was used as the processing chamber, kept off-centered on a Lindberg Blue/M single zone furnace. A 1.5-in. Cu inductor with 5 turns was fitted onto the center of the quartz tube. The end of the copper coil was connected to a 100 W tunable RF power supply through an impedance match network. The reaction system was pumped down to a base pressure of 15 mTorr, after which the chamber was purged with 20 sccm H<sub>2</sub>, maintaining an operation pressure at 300 mTorr. Plasma was generated with 15W RF power, and the visible plasma tail position was marked on the quartz tube. For the SEAR process to create WSSe, CVD grown WSe<sub>2</sub> was placed 4 cm upstream of marked visible plasma tail position onto a quartz boat, and 2 g sulfur was placed 15 cm upstream of H<sub>2</sub> plasma tail. Plasma treatment lasted for 18 min. For the creation of MoSSe, the position of CVD-grown MoSe<sub>2</sub> and S source was kept at the same position as WSSe, except processing time was decreased to 8 min because of the lower Mo-Se bond energy. The SEAR process can also be set up to create a 2D Janus structure from sulfur-based TMDs and selenium precursors in a similar fashion by varying the processing parameters (Figure 5f-j).

**PDMS-Assisted Transfer Process:** For the creation of a vertical heterostructure of Janus MoSSe/WSSe, a standard PDMS-assisted transfer process was employed.<sup>[44]</sup> A thin layer of PDMS was placed on top of CVD-grown MoSe<sub>2</sub> on SiO<sub>2</sub>, and the assembly was immersed in a 50 °C 2 M KOH solution for 1 min to etch SiO<sub>2</sub> away. The sample was then taken out and rinsed with DI water. PDMS was peeled off from SiO<sub>2</sub> and deterministically stamped on as-synthesized WSSe. After careful removal of the PDMS again, the MoSe<sub>2</sub>/WSSe was then transformed to MoSSe/WSSe by the aforementioned SEAR method.

**Raman and Photoluminescence Measurement:** Raman spectra were collected with the Renishaw Raman spectrometer with a backscattering configuration. 488 nm laser was used as the excitation source, and 1.25 mW laser power was used to pump the materials. In a typical measurement, 10 s exposure time and 3 accumulations were used. Signal was collected with 100x objective and recorded with 2400/mm grating. Photoluminescence (PL) measurement was done with the same setup except 1200/mm grating was used in the signal collection.

Low-temperature PL measurements were performed using a He-flow cryostat (Cryovac) mounted on a piezo-stage using a 633 nm and a 532 nm laser source focused to diffraction limit on the sample through a 63x long-working distance objective (N.A. = 0.75). The collected light was sent to a spectrometer (Horiba) coupled to a CCD.

**High Resolution Scanning Electron Microscopy:** Janus materials were transferred onto Quantifoil holey carbon grids with a modified PMMA-assisted process. 20–50  $\mu\text{L}$  PMMA was drop cast on the Janus supporting substrate and annealed at 120 °C. After full removal of the solvent, a PDMS support layer was placed on top to prevent the PMMA layer from wrinkling. The assembly was then immersed in a 50 °C 2 M KOH solution for 5 min to etch SiO<sub>2</sub> away. After rinsing with DI water, the PMDS–PMMA–Janus layer was removed from the supporting substrates and pressed onto the carbon grid, followed by annealing at 160 °C for 10 min. The assembly was then rinsed with 50 °C acetone to dissolve the PMMA layer, leaving Janus on the carbon grid. High-resolution scanning transmission electron microscopy was performed using aberration-corrected NION ultra STEM 100 equipped with a cold field emission gun and a fifth order aberration corrector. The microscope was operated at an accelerating voltage of 100 kV and MAADF images were taken with a convergence angle of 33 mrad, beam current of around 10–30 pA, inner collection semi-angle of 50 mrad. The sample was baked at 160° for 10 h before the experiment. The images are filtered using a Gaussian and Wiener function to remove noise and improve contrast. Images and FFT were processed by Digital Micrograph 3 software.

**Field-Effect-Transistor Device Fabrication:** CVD-grown monolayer MoSe<sub>2</sub> was transferred onto a pre-patterned 300 nm thick SiO<sub>2</sub>/Si substrate using PDMS assisted transfer method. Janus synthesis is then undertaken on this substrate using SEAR technique. Mask for electrode deposition was made by spin-coating with PMMA at 5000 RPM for 30 s. Source, drain electrodes were patterned using JEOL 6000FS Electron beam lithography, and the substrates were developed in a 3:1 IPA and MIBK solution. Contacts consisting of 5 nm Cr and 35 nm Au were deposited by Leskar 3 electron beam metal evaporator at a rate of 1 Å s<sup>-1</sup>. AZ400T stripper solution was used to do a final lift-off to obtain back-gated FET with a defined channel length of 2  $\mu\text{m}$ . After the fabrication, the devices were baked for 3 h at 150 °C under vacuum. I–V characteristics of MoSSe Janus FET can be found in Figure S14, Supporting Information.

**Density Functional Theory Calculations:** Density functional theory calculations were carried out using Vienna Ab initio Simulation Package (VASP).<sup>[46,47]</sup> The PBE functional was used to approximate the electron exchange-correlation interactions.<sup>[48]</sup> Projector-augmented wave potentials were utilized along with cut-off energy of 650 eV for the plane waves and a  $\Gamma$ -centered 15 × 15 × 1 k-point grid. The surface slab model, with a vacuum spacing of 18 Å, was used to simulate monolayer W/MoS<sub>2</sub>. The in-plane lattice constants and atomic coordinates were fully optimized to meet the force threshold of 0.01 eV Å<sup>-1</sup>. The phonon spectra were obtained from combined VASP and PHONOPY<sup>[49]</sup> calculations. The Raman spectra were calculated based on the Poezag and Pederson method.<sup>[50]</sup>

## Supporting Information

Supporting Information is available from the Wiley Online Library or from the author.

## Acknowledgements

S.T. acknowledges support from DOE-SC0020653, NSF DMR-1955889, NSF CMMI-1933214, and NSF DMR-1552220. H.Z. acknowledges the usage of computational resources from the Texas Advanced Computing Center under contract No. TG-DMR170070. The TUM groups acknowledge support from the European Union's Horizon 2020 research and innovation programme under grant agreement No. 820423 (S2QUIP) and the Deutsche Forschungsgemeinschaft

(DFG, German Research Foundation) under Germany's Excellence Strategy—MCQST (EXC-2111) and e-Conversion (EXC-2089). M.B. acknowledges support from the Alexander von Humboldt Foundation. K.M. acknowledges support from the Bavarian Academy of Sciences and Humanities. The authors acknowledge the use of facilities within the Eyring Materials Center at Arizona State University supported in part by NNCI-ECCS-1542160.

## Conflict of Interest

The authors declare no conflict of interest.

## Author Contributions

D.B.T., G.T., Y.Q., and M.Y.S. contributed equally to this work. M.B., J.J.F., K.M., and S.T. devised the project. D.B.T., S.T., and G.T. designed the growth procedures. D.B.T., Y.Q., G.T., S.Y., and M.Y.S. performed room-temperature optical characterization. H.L. calculated power density distribution in system. D.H. and S.Y. performed microscopy studies. M.B., M.P., M.M., M.K., G.S., A.V.S., J.J.F., and K.M. performed cryogenic PL measurements. M.H., L.L., and H.Z. carried out DFT calculations. I.S.E. and N.H.P. performed all the FET work. D.B.T., Y.Q., G.T., M.Y.S., and S.T. oversaw and directed the entire project. All authors participated in discussions.

## Keywords

2D materials, heterostructures, Janus structure, quantum materials

Received: September 15, 2020

Revised: October 14, 2020

Published online: November 11, 2020

- [1] Y. C. Cheng, Z. Y. Zhu, M. Tahir, U. Schwingenschlögl, *EPL* **2013**, 102, 57001.
- [2] A.-Y. Lu, H. Zhu, J. Xiao, C.-P. Chuu, Y. Han, M.-H. Chiu, C.-C. Cheng, C.-W. Yang, K.-H. Wei, Y. Yang, Y. Wang, D. Sokaras, D. Nordlund, P. Yang, D. A. Muller, M.-Y. Chou, X. Zhang, L.-J. Li, *Nat. Nanotechnol.* **2017**, 12, 744.
- [3] R. Li, Y. Cheng, W. Huang, *Small* **2018**, 14, 1802091.
- [4] J. Liang, M. Chshiev, A. Fert, H. Yang, *Phys. Rev. B* **2020**, 101, 184401.
- [5] C. Zhang, Y. Nie, S. Sanvitto, A. Du, *Nano Lett.* **2019**, 19, 1366.
- [6] J. Yuan, Y. Yang, Y. Cai, Y. Wu, Y. Chen, X. Yan, L. Shen, *Phys. Rev. B* **2019**, 101, 094420.
- [7] J. Zhang, S. Jia, I. Kholmanov, L. Dong, D. Er, W. Chen, H. Guo, Z. Jin, V. B. Shenoy, L. Shi, J. Lou, *ACS Nano* **2017**, 11, 8192.
- [8] A. Kandemir, H. Sahin, *Phys. Chem. Chem. Phys.* **2018**, 20, 17380.
- [9] Y. Wang, W. Wei, B. Huang, Y. Dai, *J. Phys.: Condens. Matter* **2019**, 31, 125003.
- [10] F. Li, W. Wei, P. Zhao, B. Huang, Y. Dai, *J. Phys. Chem. Lett.* **2017**, 8, 5959.
- [11] F. Li, W. Wei, H. Wang, B. Huang, Y. Dai, T. Jacob, *J. Phys. Chem. Lett.* **2019**, 10, 559.
- [12] K. Ishizaka, M. S. Bahramy, H. Murakawa, M. Sakano, T. Shimojima, T. Sonobe, K. Koizumi, S. Shin, H. Miyahara, A. Kimura, K. Miyamoto, T. Okuda, H. Namatame, M. Taniguchi, R. Arita, N. Nagaosa, K. Kobayashi, Y. Murakami, R. Kumai, Y. Kaneko, Y. Onose, Y. Tokura, *Nat. Mater.* **2011**, 10, 521.
- [13] J. Kang, S. Tongay, J. Li, J. Wu, *J. Appl. Phys.* **2013**, 113, 1143703.

- [14] Y.-C. Lin, C. Liu, Y. Yu, E. Zarkadoula, M. Yoon, A. A. Puretzky, L. Liang, X. Kong, Y. Gu, A. Strasser, H. M. Meyer, M. Lorenz, M. F. Chisholm, I. N. Ivanov, C. M. Rouleau, G. Duscher, K. Xiao, D. B. Geohegan, *ACS Nano* **2020**, *14*, 3896.
- [15] S. Tongay, J. Suh, C. Ataca, W. Fan, A. Luce, J. S. Kang, J. Liu, C. Ko, R. Raghunathanan, J. Zhou, F. Ogletree, J. Li, J. C. Grossman, J. Wu, *Sci. Rep.* **2013**, *3*, 2657.
- [16] S. Tongay, W. Fan, J. Kang, J. Park, U. Koldemir, J. Suh, D. S. Narang, K. Liu, J. Ji, J. Li, R. Sinclair, J. Wu, *Nano Lett.* **2014**, *14*, 3185.
- [17] Y.-H. Lee, X.-Q. Zhang, W. Zhang, M.-T. Chang, C.-T. Lin, K.-D. Chang, Y.-C. Yu, J. T.-W. Wang, C.-S. Chang, L.-J. Li, T.-W. Lin, *Adv. Mater.* **2012**, *24*, 2320.
- [18] J. Zhou, J. Lin, X. Huang, Y. Zhou, Y. Chen, J. Xia, H. Wang, Y. Xie, H. Yu, J. Lei, D. Wu, F. Liu, Q. Fu, Q. Zeng, C.-H. Hsu, C. Yang, L. Lu, T. Yu, Z. Shen, H. Lin, B. I. Yakobson, Q. Liu, K. Suenaga, G. Liu, Z. Liu, *Nature* **2018**, *556*, 355.
- [19] X. Wang, Y. Li, L. Zhuo, J. Zheng, X. Peng, Z. Jiao, X. Xiong, J. Han, W. Xiao, *CrystEngComm* **2018**, *20*, 6267.
- [20] H.-C. Lee, *Appl. Phys. Rev.* **2018**, *5*, 011108.
- [21] F. Lei, X. Li, Y. Liu, D. Liu, M. Yang, Y. Yu, *AIP Adv.* **2018**, *8*, 015003.
- [22] J. Kang, S. Tongay, J. Zhou, J. Li, J. Wu, *Appl. Phys. Lett.* **2013**, *102*, 1012111.
- [23] S.-Z. Yang, Y. Gong, P. Manchanda, Y.-Y. Zhang, G. Ye, S. Chen, L. Song, S. T. Pantelides, P. M. Ajayan, M. F. Chisholm, W. Zhou, *Adv. Mater.* **2018**, *30*, 1803477.
- [24] S.-Z. Yang, W. Sun, Y.-Y. Zhang, Y. Gong, M. P. Oxley, A. R. Lupini, P. M. Ajayan, M. F. Chisholm, S. T. Pantelides, W. Zhou, *Phys. Rev. Lett.* **2019**, *122*, 106101.
- [25] X. Duan, C. Wang, Z. Fan, G. Hao, L. Kou, U. Halim, H. Li, X. Wu, Y. Wang, J. Jiang, A. Pan, Y. Huang, R. Yu, X. Duan, *Nano Lett.* **2015**, *16*, 264.
- [26] Y. Gong, Z. Liu, A. R. Lupini, G. Shi, J. Lin, S. Najmaei, Z. Lin, A. L. Elías, A. Berkdemir, G. You, H. Terrones, M. Terrones, R. Vajtai, S. T. Pantelides, S. J. Pennycook, J. Lou, W. Zhou, P. M. Ajayan, *Nano Lett.* **2013**, *14*, 442.
- [27] Q. Feng, Y. Zhu, J. Hong, M. Zhang, W. Duan, N. Mao, J. Wu, H. Xu, F. Dong, F. Lin, C. Jin, C. Wang, J. Zhang, L. Xie, *Adv. Mater.* **2014**, *26*, 2648.
- [28] H. Li, Y. Qin, B. Ko, D. B. Trivedi, D. Hajra, M. Y. Sayyad, L. Liu, S. H. Shim, H. Zhuang, S. Tongay, *Adv. Mater.* **2020**, *32*, 2002401.
- [29] K. F. Mak, K. He, C. Lee, G. H. Lee, J. Hone, T. F. Heinz, J. Shan, *Nat. Mater.* **2013**, *12*, 207.
- [30] S. Tongay, J. Suh, C. Ataca, W. Fan, A. Luce, J. S. Kang, J. Liu, C. Ko, R. Raghunathanan, J. Zhou, F. Ogletree, J. Li, J. C. Grossman, J. Wu, *Sci. Rep.* **2013**, *3*, 2657.
- [31] Y. P. Varshni, *Physica* **1967**, *34*, 149.
- [32] S. Tongay, J. Zhou, C. Ataca, K. Lo, T. S. Matthews, J. Li, J. C. Grossman, J. Wu, *Nano Lett.* **2012**, *12*, 5576.
- [33] N. Lundt, A. Maryński, E. Cherotchenko, A. Pant, X. Fan, S. Tongay, G. Sek, A. V. Kavokin, S. Höfling, C. Schneider, *2D Mater.* **2016**, *4*, 015006.
- [34] J. Huang, T. B. Hoang, M. H. Mikkelsen, *Sci. Rep.* **2016**, *6*, 22414.
- [35] Z. Li, T. Wang, C. Jin, Z. Lu, Z. Lian, Y. Meng, M. Blei, S. Gao, T. Taniguchi, K. Watanabe, T. Ren, S. Tongay, L. Yang, D. Smirnov, T. Cao, S.-F. Shi, *Nat. Commun.* **2019**, *10*, 2469.
- [36] J. P. Echeverry, B. Urbaszek, T. Amand, X. Marie, I. C. Gerber, *Phys. Rev. B* **2016**, *93*, 121107.
- [37] G. Wang, C. Robert, A. Suslu, B. Chen, S. Yang, S. Alamdar, I. C. Gerber, T. Amand, X. Marie, S. Tongay, B. Urbaszek, *2015*, *6*, 10110.
- [38] W. Bao, N. J. Borys, C. Ko, J. Suh, W. Fan, A. Thron, Y. Zhang, A. Buyanin, J. Zhang, S. Cabrini, P. D. Ashby, A. Weber-Bargioni, S. Tongay, S. Aloni, D. F. Ogletree, J. Wu, M. B. Salmeron, P. J. Schuck, *Nat. Commun.* **2015**, *6*, 7993.
- [39] D. Er, H. Ye, N. C. Frey, H. Kumar, J. Lou, V. B. Shenoy, *Nano Lett.* **2018**, *18*, 3943.
- [40] A. C. Riis-Jensen, M. Pandey, K. S. Thygesen, *J. Phys. Chem. C* **2018**, *122*, 24520.
- [41] C. Huang, S. Wu, A. M. Sanchez, J. J. P. Peters, R. Bearland, J. S. Ross, P. Rivera, W. Yao, D. H. Cobden, X. Xu, *Nat. Mater.* **2014**, *13*, 1096.
- [42] F. Wang, J. Wang, S. Guo, J. Zhang, Z. Hu, J. Chu, *Sci. Rep.* **2017**, *7*, 44712.
- [43] A. Castellanos-Gomez, M. Buscema, R. Molenaar, V. Singh, L. Janssen, H. S. J. van der Zant, G. A. Steele, *2D Mater.* **2014**, *1*, 011002.
- [44] A. Jain, P. Bharadwaj, S. Heeg, M. Parzefall, T. Taniguchi, K. Watanabe, L. Novotny, *Nanotechnology* **2018**, *29*, 265203.
- [45] B. Yorulmaz, A. Özden, H. Sar, F. Ay, C. Sevik, N. K. Perkgöz, *Mater. Sci. Semicond. Process.* **2019**, *93*, 158.
- [46] G. Kresse, J. Furthmüller, *Phys. Rev. B* **1996**, *54*, 11169.
- [47] G. Kresse, J. Hafner, *Phys. Rev. B* **1993**, *47*, 558.
- [48] J. P. Perdew, K. Burke, M. Ernzerhof, *Phys. Rev. Lett.* **1996**, *77*, 3865.
- [49] A. Togo, I. Tanaka, *Scr. Mater.* **2015**, *108*, 1.
- [50] D. Porezag, M. R. Pederson, *Phys. Rev. B* **1996**, *54*, 7830.